

Andromeda's tenuous veil: extensive nebular emission near (yet far from) M31

A. Lumbreras-Calle^{1,*}, J. A. Fernández-Ontiveros^{1,2}, R. Infante-Sainz¹, M. Akhlaghi^{1,2}, B. Montoro-Molina³, B. Pérez-Díaz³, A. del Pino^{1,2,3}, H. Vives-Arias¹, A. Hernán-Caballero^{1,2}, C. López-Sanjuan^{1,2}, M. A. Guerrero³, S. Eskandarlou¹, and A. Ederoclite^{1,2}

¹ Centro de Estudios de Física del Cosmos de Aragón (CEFCA), Plaza San Juan 1, 44001 Teruel, Spain

² Unidad Asociada CEFCA-IAA, CEFCA, Unidad Asociada al CSIC por el IAA, Plaza San Juan 1, 44001 Teruel, Spain

³ Instituto de Astrofísica de Andalucía (IAA-CSIC), P.O. Box 3004, 18080 Granada, Spain

ABSTRACT

Context. A large, faint nebula was unexpectedly discovered near M31 using narrowband [O III] images. Its apparent size and the lack of a clear counterpart at other wavelengths make it unique and challenging to explain.

Aims. We aim to determine whether the nebula is extragalactic and vast or associated with the Milky Way filamentary structure. This will enable us to constrain its physical properties and assess its nature.

Methods. We obtained deep narrowband [O II]3727 and H α + [NII] observations with the JAST80 telescope at the Observatorio Astrofísico de Javalambre, as well as very high-spectral-resolution spectroscopy at four locations within the region of interest using the MEGARA integral field unit at the Gran Telescopio Canarias.

Results. We found extended [O II] emission along two near-parallel strands to the [O III], offset by six arcmin. The nebular spectra reveals up to 6 emission lines from [O III]4959,5007, H β , [N II]6583, and [S II]6716,6731. Their receding velocities are above -40 km s⁻¹, far from the systemic velocity of M31 (-300 km s⁻¹). The fluxes and velocities are remarkably consistent for the same lines across different regions of the nebula.

Conclusions. The nebular properties suggest a location within the Milky Way rather than being physically associated with M31. The most likely scenario suggests a resolved ionization structure in a Galactic nebula with a separation between [O II] and [O III] of the order of a few parsecs. The observed receding velocities would be unprecedented for an object physically linked to M31 but are common for nearby gas filaments. Their consistency across the nebula would also be highly unusual if it were larger than a kiloparsec. The analysis of the emission-line ratios, line widths, and morphology suggests the possibility of it being an interstellar gas filament with an additional source of ionization to explain the [O III] emission. However, the complex properties of this object call for further observations to confirm its nature.

1. Introduction

Since the middle of the 20th century, in addition to broad band imaging, the sky has been observed with surveys focused on studying nebular line emission. Early examples were blind surveys performed with objective prisms, unveiling large numbers of galactic objects such as planetary nebulae and supernova remnants (Minkowski 1946), a technique also applied to the discovery of extragalactic objects such as emission line galaxies (Markaryan 1967; MacAlpine et al. 1977). Narrow band photometry was also developed early, mostly focused on H α observations of galactic objects (Shajn & Gaze 1952; Gum 1953) but also nearby galaxies (Shajn & Gaze 1952; Courtes 1952). Many more surveys, focusing on H α within our own Galaxy, have continued this work, such as the Virginia Tech Spectral-line Survey (VTSS; Dennison et al. 1998) and IPHAS (Drew et al. 2005). One early example of galactic survey targeting other optical emission lines was Parker et al. (1979), leading to the discovery of multiple planetary nebulae. The Wisconsin H α Mapper survey (WHAM; Haffner et al. 2003) has primarily observed spectroscopically in the H α wavelength range, with some fields covered in other emission lines), providing high spectral resolution over wide areas of the sky.

Beyond our galaxy, the systematic surveys performed over the past two decades using narrowband filters have only tar-

geted small areas of the sky, focusing mainly on compact objects at intermediate and high redshifts (i.e. Cardamone et al. 2010; Moles et al. 2008; Pérez-González et al. 2013; Taniguchi et al. 2015). Using large scale, broadband surveys, only a few extreme examples of extended, ionized structures beyond the local group have been discovered, the most notable being Extended Emission Line Regions (EELRs; Lintott et al. 2009; Keel et al. 2012). With a stronger discovery potential for these kinds of structures, several recent narrowband projects are targeting large sky areas, such as the Merian survey (Danieli et al. 2024), the Javalambre Photometric Local Universe Survey (J-PLUS; Cernaro et al. 2019), the Southern Photometric Local Universe Survey (S-PLUS; Mendes de Oliveira et al. 2019), and the Javalambre Physics of the Accelerated Universe Survey (J-PAS; Benítez et al. 2014; Bonoli et al. 2021). They have already yielded results, for example, on extended Lyman α emission around quasars (Rahna et al. 2022), jellyfish galaxies (Gondhalekar et al. 2024), and nearby extreme emission line galaxies (Lumbreras-Calle et al. 2022).

Despite the long history of observations of emission line objects, there remains a large potential for new discoveries. The low surface brightness (LSB) regime has been poorly explored due to observational constraints, especially targeting emission lines. In the more distant Universe, integral field unit (IFU) spectroscopy has been used in the past decade to measure faint emission line structures. Using the MUSE IFU, with data from the

* e-mail: alumbrerascalleg@gmail.com

Multi Unit Spectroscopic Explorer (MUSE) Ultra Deep Field (Bacon et al. 2017), extended Lyman α emission was identified around most distant galaxies (Wisotzki et al. 2018), and it was also found to trace the cosmic web structure (Bacon et al. 2021). Using stacking techniques, deep MUSE data was used as well to detect H α emitting sources near galaxies (likely intermediate-mass black holes) or to measure the extended line emission around galaxies (Dutta et al. 2024).

In the nearby Universe, however, there is still a lack of deep, wide observations of emission lines over wide fields. Amateur astronomers, targeting relatively wide areas of the sky for hundreds of hours, are able to obtain deeper observations than what is available in the scientific literature for specific fields. One example of these projects is the one leading up to the discovery of a large nebula near M31. It was detected by amateur astronomers observing with a narrowband [O III]5007 filter (Drechsler et al. 2023), and they named it Strottner-Drechsler-Sainty Object (SDSO). The nebula is very faint, with [O III] surface brightness of $\sim 10^{-18}$ erg s $^{-1}$ cm $^{-2}$ arcsec $^{-2}$, yet is very large (~ 1.5 deg) and presents a filamentary structure. One of its most striking features was an apparent lack of any counterpart, neither in H α emission, nor in X-ray, UV, optical, or infrared observations. In Fesen et al. (2023), the photometric data is described in more detail, and additional spectroscopic follow-up is presented, using the Ohio State Multi-Object Spectrograph (OSMOS) at the MDM 2.4m Hiltner telescope. It showed a receding velocity of ~ -10 km s $^{-1}$. Despite this, in an extensive and detailed analysis, they conclude that the nebula is unlikely to be located within the Milky Way by ruling out its classification into several classes of galactic objects. They favor the view that the nebula is in the M31 halo instead, ionized by shocks. Amram et al. (2023) also performed spectroscopic observations with MISTRAL at the Haute-Provence Observatory 193 cm telescope, with discrepant results (a receding velocity of ~ -100 km s $^{-1}$).

In this work, we present additional photometric and spectroscopic observations of the nebula. We discuss possible scenarios for its location and physical nature, comparing with different classes of objects and taking into account the available data. This paper is structured as follows: In Section 2 we describe our observations. In Section 3, we present the direct results of the observations and the measurements we performed on them. In Section 4, we discuss the implications of the results, comparing with the literature to infer the most likely location and physical nature of the nebula. In Section 5 we summarize our conclusions.

2. Observational data

We secure follow-up observations on the M31 [O III] nebula to constrain its possible physical properties and determine its galactic or extragalactic nature. More specifically, we obtained narrowband photometry targeting both the [O II] and H α emission lines, and integral field spectroscopy covering the ranges from H β to [O III]5007 and from H α to [S II]6731. In this Section we present each of these datasets within their respective subsections.

2.1. OAJ photometric observations

In order to explore the morphology of the nebula in other optical emission lines, we obtained photometric observations with the Javalambre Auxiliary Survey Telescope (JAST80), an 80 cm telescope located at the Observatorio Astrofísico de Javalambre (OAJ), thanks to its Director Discretionary Time (DDT) program, through proposal 2300222 (P.I. Lumbrales-Calle). The

camera (T80Cam) is optimal for wide field imaging, thanks to its $9.2\text{k} \times 9.2\text{k}$ CCD, with a pixel scale of 0.55 arcsec pix $^{-1}$, resulting in a Field of View (FoV) of $1.4^\circ \times 1.4^\circ$. Its primary task is to perform J-PLUS (Cenarro et al. 2019), a 8500 deg 2 photometric multiband survey using a set of 12 filters (5 wide, and 7 narrow-medium).

Besides the [O III]5007 and H α emission lines, the other optical emission lines that may be relatively strong and which trace gas with different properties are the [O II]3727 doublet and the [N II]6583 and [S II]6716,6731 lines, since these lines are an important mechanism for the nebula to cool down and given the standard abundances of oxygen, nitrogen and sulfur (e.g. Kobayashi et al. 2020). Considering the available filters at the T80cam in JAST80, and the presence of H α near [N II]6583, we proposed observations using the J0378 filter ($\lambda_{eff}=3793.4$ Å, $W_{eff}=136.3$ Å) which covers the [O II]3727 emission line. We also observed the nebula with the J0660 filter ($\lambda_{eff}=6606.9$ Å, $W_{eff}=146.6$ Å), covering both the H α and [N II]6548,6583 emission lines. This allows us to compare our JAST80 images with the existing observations in Drechsler et al. (2023); Fesen et al. (2023) and our spectra.

To facilitate the data reduction process and the detection of LSB structures, we used a large dithering pattern of about half a degree. We implemented this by defining four separate pointings, each one with an additional, smaller dithering pattern of 10 arcsec. Since the maximum exposure time for this instrument is 600 s (10 minutes), we proposed to perform 6 individual observations in each pointing for the J0378 image, and 3 for J0660. However, given the short time frame available to secure all observations due to M31 visibility, one of the pointings in the J0660 was not observed, and two exposures in one of the J0378 pointings are missing as well. We secured therefore 22 individual 600 s images in J0378 for a total of 13200 s (3.67 hours) of exposure in the central region, and 9 images for a total of 5400 s (1.5 hours) of exposure in J0660. The different pointings performed only overlap in the central area, of roughly 56 arcmin \times 50.3 arcmin (0.78 deg 2), which covers most of the [O III] nebula, as shown in Fig. 1

The raw exposures were processed by the data processing and archival department (DPAD) at CEFCA. The standard J-PLUS pipeline was used to perform the bias and flat field corrections and flux calibration. In addition to that, during the sky background correction step, special care was taken in order to avoid the removal of potential LSB structures on the images. To do this, the Gnuastro NoiseChisel program (Akhlaghi & Ichikawa 2015; Akhlaghi 2019a) was used to accurately detect all significant objects in the image without any parametric fitting to their profiles, and to estimate a non-parametric model of the sky background. With this program it is possible to detect very faint signal from LSB features (i.e., the faint nebulae) and mask them, to keep them in the final images and avoid incorrectly subtracting them as the sky background. The final models of the sky background emission were estimated by fitting the NoiseChisel sky tiles (before interpolation) with 2-dimensional Chebyshev polynomials (order=3 for J0378, and order=4 for J0660) to the previous sky background models. After subtracting the sky background emission, all individual frames were resampled into the same common grid and sigma-clipped and mean-stacked to obtain the co-added images.

In order to remove the contamination of the scattered light from the very bright stars on the co-added images, the extended point spread function (PSF) was estimated. The method we followed is described in detail in Infante-Sainz et al. (2020). In

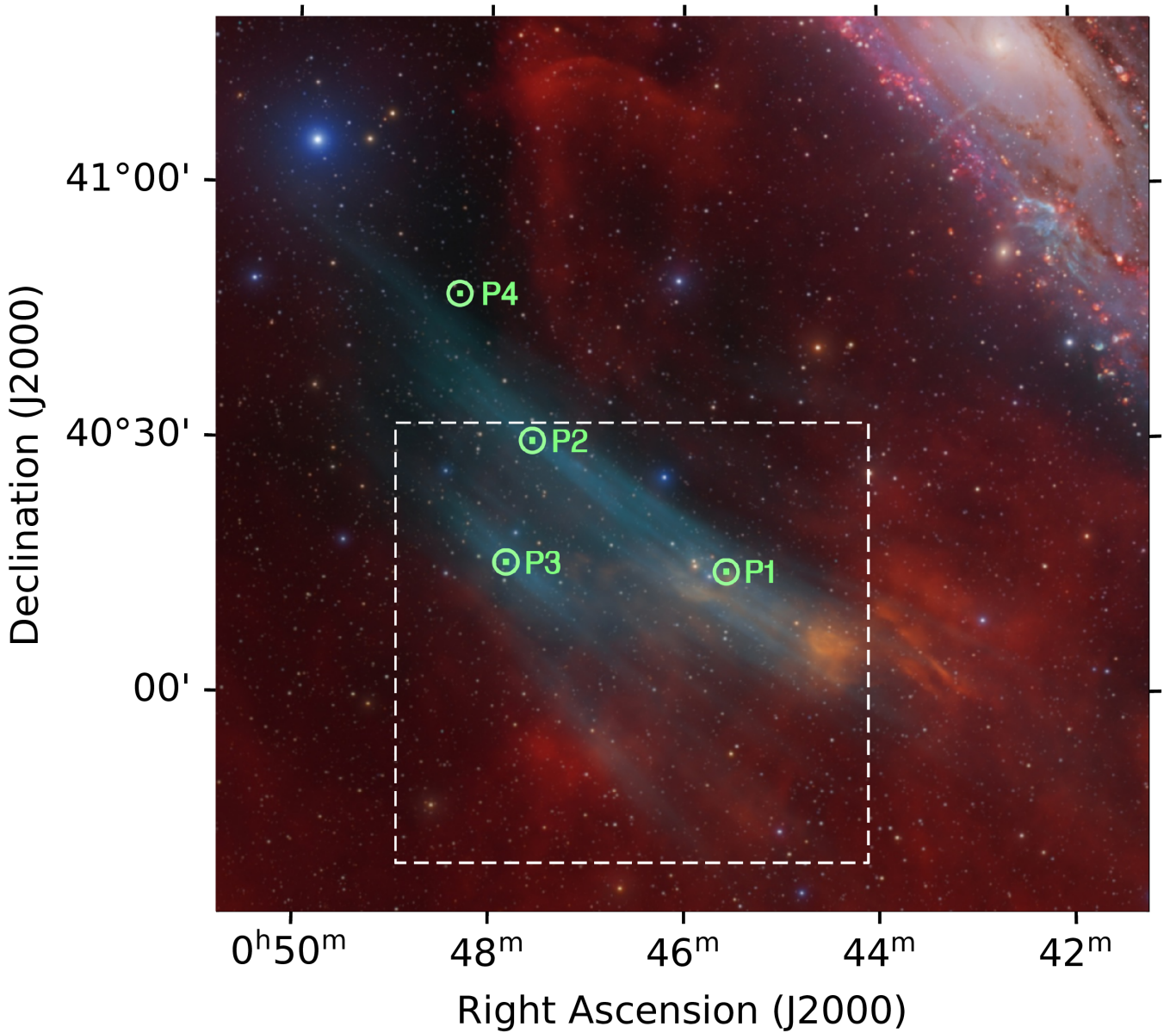


Fig. 1. Image of the [O III] emitting nebula (known as SDO) and its surrounding area, including the Andromeda galaxy (top right). The [O III] flux is shown in cyan, while $H\alpha + [N II]$ is shown in red. The green squares (surrounded by green circles) mark the location of the MEGARA pointings in and around the nebula presented in this work. The dashed square shows the area covered by our full-depth observations with the JAST80 telescope targeting [O II] and $H\alpha$ with narrowbands J0378 and J0660, respectively. The RGB image¹ of the nebula and M31 was presented in Drechsler et al. (2023), and was obtained by Marcel Dreschler, Xavier Strottner, and Yann Sainty.

short, very bright stars (Gaia Collaboration 2020, $G < 10$ mag) were processed and stacked to measure the far extended wings of the PSF (up to a radius of ~ 3 arcmin). Fainter and non-saturated stars ($G = 10 - 14$ mag) were used for the core of the PSF, and both of these sources were combined into a single extended PSF model. This model was then subtracted from the bright stars ($G < 14$ mag) in the images to remove their scattered light and avoid contamination of LSB structures. For fainter stars ($G > 14$ mag) this procedure was not applied, since their brightness does not extend very far away. They were simply detected and masked instead. Finally, with the goal of increasing the signal-to-noise (S/N) ratio of faint structures, the pixel scale of the images was increased to $20 \text{ arcsec pix}^{-1}$.

The final results after the data reduction process are shown in Fig. 2. We have considered only the region where we reach the full depth, a rectangle of 56 arcmin by 50 arcmin of size, giving a total area of 2750 arcmin^2 or 0.75 deg^2 .

2.2. MEGARA spectroscopic observations

To accurately measure the receding velocity of the nebula and assess its physical state, we have obtained spectroscopic observations using the IFU mode of the Multi-Espectrógrafo en GTC de Alta Resolución para Astronomía (MEGARA) instrument mounted at the 10.4m Gran Telescopio Canarias (GTC) in the Observatorio Astronómico del Roque de los Muchachos (ORM). We secured observing time through the DDT program GTC2023-206 (P.I. Lumbreras-Calle). We targeted 3 different regions in the nebula (P1, P2, and P3) and one outside of its ap-

¹ <https://www.astrobin.com/1d8ivk/0/>

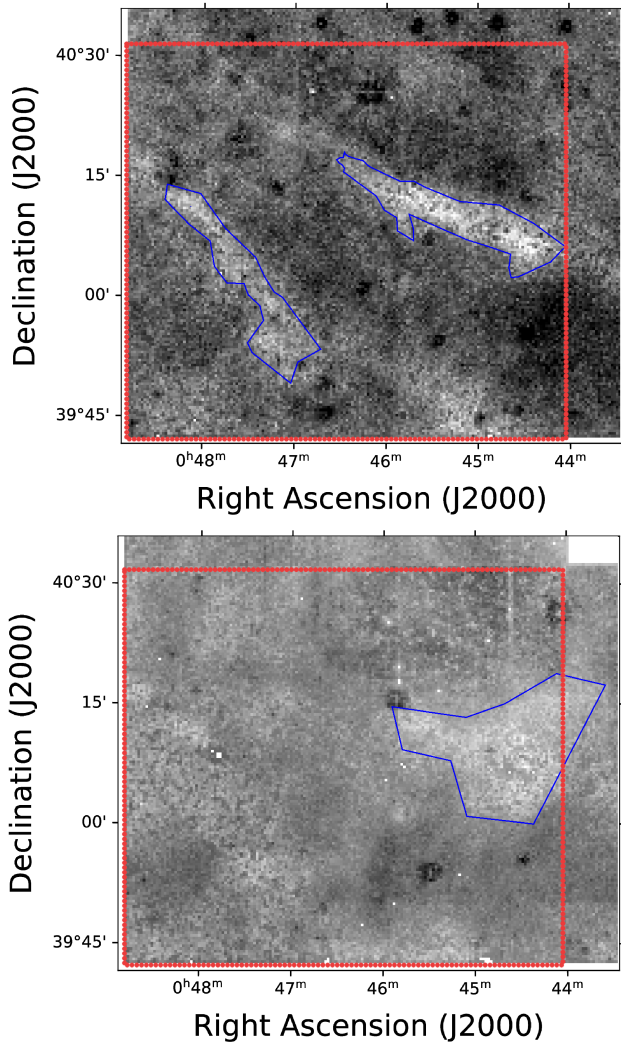


Fig. 2. Narrowband images obtained using JAST80 on the [O III] nebula. *Top.* J0378 image, tracing the [O II]3727 emission line. *Bottom.* J0660 image, tracing $H\alpha$ and [N II] emissions. In both images, in blue, we show the contours of areas where we detect emission in each image. In dotted, red lines, we encircle the area where the full depth in the images is achieved.

Table 1. Central position of the MEGARA pointings.

Pointing	RA [deg]	DEC [deg]
P1	11.3792	40.2435
P2	11.8913	40.4936
P3	11.9480	40.25428
P4	12.0784	40.7820

parent footprint (P4; see Fig. 1). The pointings P1 and P2 were selected along the major axis of the object, focusing on regions with significant [O III] emission, and at least one (P1) where the $H\alpha$ emission was noticeable as well. P3 was selected in a separate “strand” of the nebula, along what could be considered its minor axis. The precise central coordinates of the pointings are listed in Table 1, and were chosen to avoid any other visible source within the footprint of the MEGARA IFU (approximately 12.5×11.3 arcsec) to minimize contamination.

To increase the S/N in the spectra, and to potentially detect multiple emission lines to determine physical properties,

we used the lowest resolution dispersion elements available in MEGARA, since they would still be enough to perform accurate velocity measurements ($R \geq 5000$). The Volume Phase Holographic (VPH) dispersion elements we used to cover the wavelength range of [O III] was VPH480-LR (LR-B), ranging from 4332.05 \AA to 5199.96 \AA , with a pixel scale of $0.207 \text{ \AA pix}^{-1}$. In addition, we observed pointings P1, P2, and P4 with VPH675-LR (LR-R), ranging from 6096.54 \AA to 7303.21 \AA and a pixel scale of $0.287 \text{ \AA pix}^{-1}$, to cover the wavelength range of $H\alpha$, [N II] and [S II]. Distinguishing between different ionizing sources requires the simultaneous analysis of both high-ionized ions (e.g. [O III]) and low-ionized species (e.g. [N II], [S II]). Additionally, the information from the [S II] doublet is needed to constrain the electron density of the nebula.

The observations were observed in two nights, 2023/01/21 and 2023/01/23. In each night, the same observation sequence was performed. For pointings P1 and P2, three exposures of 600 s in each VPH were taken. In P3, only observations in LR-B were taken, and in P4, only 1 exposure in each VPH was taken. Since the object is much more extended than the MEGARA IFU, we placed no constraints in the seeing, and the observations were taken under filler conditions.

The data were reduced using the MEGARA data reduction pipeline, *megaradrp*, version 0.12.0 (Pascual et al. 2021). Briefly explained, the procedure starts by subtracting the bias level from the raw FITS files, and then the individual spectra from each fiber have to be traced across the 2D images. This is done using the flat observations, where the trace of each fiber is very clear. Then, the flux from each fiber is calibrated in wavelength, using arc-lamp observations. Finally, each fiber is corrected from the differential sensitivity across wavelength with a flat-field correction. For the final results, we combined the three exposures that were taken for each nebula pointing with each VPH. The only exceptions were the LR-B observations of the P1 pointing. Those were performed early after twilight in both nights, and this led to the contamination of the spectra by sunlight, showing significant absorption lines that prevented us from accurately measuring the emission lines of the nebula, especially [O III]4959 and $H\beta$. Therefore for this pointing, in both nights, we only used the third frame taken, which showed almost no sunlight effect.

The only difference in our data reduction process from the standard is that we did not perform sky subtraction. In MEGARA this process is performed by removing from the science data the flux measured by dedicated fibers located at $\sim 1.75 - 3$ arcmin from the IFU. Given the large size of our target, those sky fibers are contaminated by the nebular emission, therefore using them to subtract the sky would remove the very emission lines we intend to detect. Our original plan to perform sky subtraction was to use the pointing outside the footprint of the nebula (P4), but that data was also contaminated by nebular emission lines, and therefore we performed no sky subtraction. Since we are expecting to only detect the emission lines from the nebula and not the continuum, our only concern are sky emission lines. They do not affect the nebular lines in the blue range of the spectrum, and only contaminate the $H\alpha$ in the red range (we will address this in Section 3.2.1).

Using the observations of a standard star each night we performed flux calibration with the MEGARA pipeline. The final product of the data reduction was therefore a flux-calibrated 2D spectrum with one row per fiber. The main science-ready output we extracted from it was a 1D spectrum obtained by taking the median of all rows. The only correction at this stage was to re-

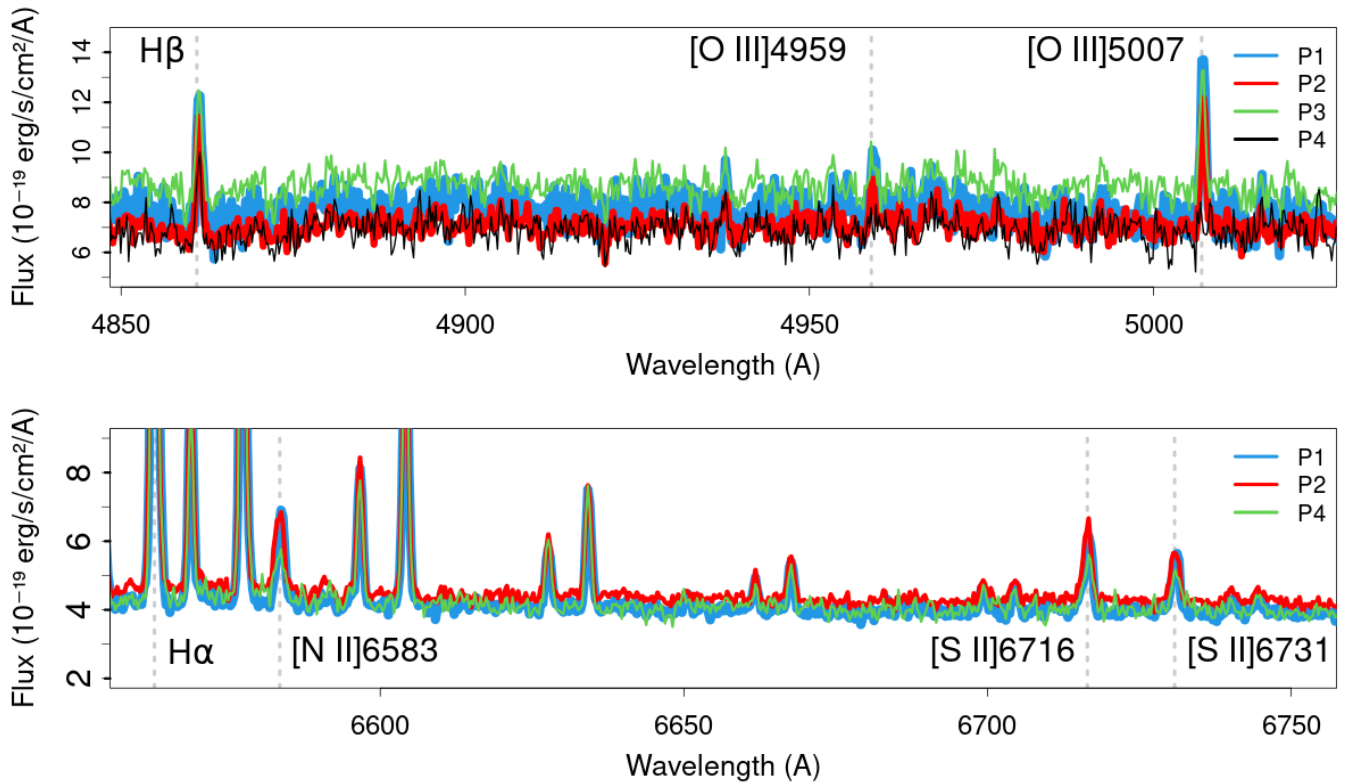


Fig. 3. MEGARA spectra of the pointings in the first night (four in the blue range, three in the red), in the observed wavelength frame. *Top.* The LR-B spectra, centered in the wavelength range from H β to [O III] 5007. *Bottom.* The LR-R spectra, from [N II] 6583 to [S II] 6731. The emission lines of interested are marked in both plots. The lines that are not marked are sky emission lines, with H α being contaminated by one.

move the sky fibers from the median to avoid mixing different regions of the nebula. We also explored the possibility of detecting variations of emission within each pointing, by dividing the field into 9 equal squares arranged in a 3x3 pattern, but found no significant changes. The final reduced spectra for all pointings in the first night and both VPHs are shown in Fig. 3, focusing on the wavelength ranges of interest in this work.

3. Results

In this Section we describe the outcome of our observations. We first describe the results of the JAST80 imaging in two narrowbands. Then, we present the results of the spectroscopic observations targeting the nebula, describing the velocity, width, and flux of the different emission lines.

3.1. Photometry

After the data reduction of the images taken at the OAJ (presented in 2.1) we obtained the images in Fig. 2. The top panel shows the image taken with the J0378 filter, tracing the emission from the [O II] 3727 doublet, while the bottom panel image corresponds to the J0660 filter and shows H α and [N II] 6548,6586 emission. In both of the images we successfully detect low surface brightness structures in the area where the [O III] nebula was detected.

In the [O II] image, (see top panel in Fig. 2), we can identify clearly two separate elongated structures. The brighter one, on the west, is approximately 4 arcmin wide and 30 arcmin long, while the fainter, at the south-east, is slightly smaller (27 arcmin) and thinner (3.7 arcmin).

For the brighter one, the median surface brightness is 27.8 mag arcsec⁻² (7.8 erg s⁻¹ cm⁻² arcsec⁻², assuming all the flux comes from the emission line), with a total integrated magnitude of 13.6 mag. The fainter shows 28.0 mag arcsec⁻² (6.5 erg s⁻¹ cm⁻² arcsec⁻²) and 14 mag. For simplicity, we have performed our measurements on manually defined apertures, but moderate changes would not affect the results significantly (for example, a 60% increase in the size of the lower region would result in just a 5% decrease in surface brightness). Since these structures are very faint, we have pushed the images to their surface brightness limits. This resulted in the reveal of some systematic effects, and the estimation of the significance of the detections therefore requires special care. A simple analysis, pixel by pixel, of the S/N would overestimate it, overlooking the large scale systematic effects (such as the circular dark regions visible across the image, corresponding to the removal of stars). To overcome that, we performed flux measurements in 10000 apertures with the same shape and size of the ones we have used to make the measurements, but randomly placed all around the image, using the `-upperlimit-sigma` column of Gnuastro's `MakeCatalog` program (Akhlaghi 2019b). This process then takes the width of the distribution of those 10000 fluxes as an upper limit to the uncertainty in the flux values in our regions of interest. Depending on where we allow these random apertures to be placed, the S/N gives different values. If we only avoid placing them on the aperture of the region we are considering (thus assuming that everything but the region of interest is noise), we obtain values of S/N = 5.1 in the first region and 5.9 in the second. If we mask every detection in the image using `Noisechisel`, this S/N value goes up to 13.3 and 13.4, respectively. The fainter structure shows higher S/N due to its orientation, which is not aligned with the

linear structures that seem to cross the whole image. In any case, this test demonstrates that these structures are confidently detected above the 5σ level.

In the $H\alpha$ image we detect a roughly triangular region of ~ 24 - 27 arcmin in size. The median surface brightness in that structure is $27.05 \text{ mag arcsec}^{-2}$ ($5.5 \text{ erg s}^{-1} \text{ cm}^{-2} \text{ arcsec}^{-2}$). With the same method explained earlier in this section, the S/N ranges from 5.3 to 6.7, confirming the reality of this structure.

3.2. Spectroscopy

To extract physical information from the spectra we run a custom-made code to measure the key properties of the emission lines, which we describe in this Section. After visual inspection, we focused only in the clearly detected lines: $H\beta$, $[O III]\lambda 4959$, $[O III]\lambda 5007$ in LR-B, and $[N II]\lambda 6548$, 6583 , $H\alpha$, and $[S II]\lambda 6716$, 6731 . As a reference for calibration, we also measured the four strongest sky emission lines found closer in wavelength to the nebular emission lines. The code estimates the continuum level within a $\pm 1500 \text{ km s}^{-1}$ range centered on the line wavelength, masking the $\pm 120 \text{ km s}^{-1}$ region around the line. Minor adjustments to these ranges were made for specific lines when contamination from an adjacent spectral feature or sky line was present. For each line, a first-degree polynomial was fitted to the defined continuum range and then subtracted from the spectrum. A Gaussian function was fitted to the line profiles in the continuum-subtracted spectrum to derive the flux, central wavelength, velocity with respect to the rest-frame wavelength, and line width. The line fluxes and best-fit parameters are shown in Table 2. Upper limits correspond to 3σ , where σ is the associated uncertainty of the fit. Further corrections applied to the output values from the code are explained in the following subsections.

We successfully detect the $[O III]\lambda 5007$ and $H\beta$ emission lines in all our MEGARA pointings in the nebula (P1, P2, and P3), confirming the initial result in Drechsler et al. (2023) (Fig. 3).

3.2.1. Emission line fluxes

The flux-calibrated 1D spectra obtained for each pointing and night described in Section 2.2 were the median of all fibers. To transform it into surface brightness, we divided the flux by the area of one fiber (0.2497 arcsec^2 , since it is a hexagon with a maximum diameter of 0.62 arcsec). These fluxes are presented in Fig. 4.

We have excluded from our analysis (and thus from Fig. 4) the line fluxes measured in the second night, since no flatfield observations were performed. Using the flat from the night after that one results in a poor calibration, presenting large scale fluctuations in the flux values across wavelength, with significant slope in regions that showed none the first night. This, as we have shown, does not affect the wavelength calibrations, since we obtained remarkably similar velocity values for the same lines in both days. Even considering this issue, the flux values are reasonably consistent from the first night to the second night in most cases (13 out of the 16 lines detected in both nights are compatible within the uncertainties).

We consider that the absolute flux values may hold uncertainties unaccounted for in the stated error intervals. Performing such a calibration over large wavelength ranges is sometimes challenging in spectra, but in this instance it is more complex given the unusual instrument mode (integrating all flux from the

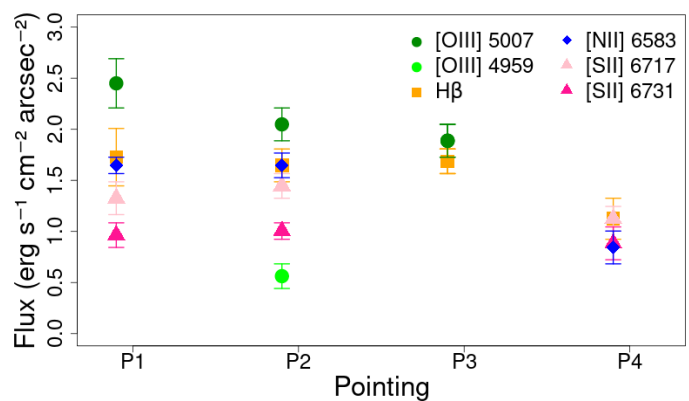


Fig. 4. Line fluxes measured with MEGARA at GTC in the different pointings in the region of the nebula on the first night of observations. They correspond to the integrated flux of the best fitting Gaussian function to the line profile. The lines that are missing have not been detected by our code in the spectra, except for the red lines ($\lambda > 6000 \text{ \AA}$) in P3, since there were no observations to fit.

587 fibers), and the very faint and extended nature of the object. Nevertheless, the calibration shows consistent results between pointings, nights, and across different observations.

We cannot, however, separate the $H\alpha$ flux in our pointings from the very strong sky emission line at 6562.76 \AA . The flux of this line varies from one pointing and night to the other, in contrast with other sky emission lines, and that change is likely attributable to $H\alpha$ from the nebula. But the variations are not consistent with the distribution of $H\alpha$ flux in the images, or from the first night to the second one. Any conclusion drawn from what is already a heavily contaminated line would be very uncertain.

3.2.2. Velocity derived from the emission lines

After performing the Gaussian fit to the emission lines, our code also outputs the difference between each measured line and its rest-frame wavelength, in units of km s^{-1} , for all lines and pointings in both days. The errors are very low: on the order of $2 - 3 \text{ km s}^{-1}$ for the nebula emission lines and below 1 km s^{-1} for the much stronger sky emission lines. For the latter, the velocity shift should be compatible with zero in all cases, since they come from our own atmosphere. Nevertheless, we measure differences much larger than the errors, from -5.9 km s^{-1} to $+3.5 \text{ km s}^{-1}$. These shifts are not random but correlated, being for example all positive on the first night and negative on the second night, and similar for different lines in each specific pointing. This indicates that the wavelength calibration is not stable enough across pointings or nights to directly compare the velocity shifts of the nebula emission lines. In order to correct for this effect, we have simply subtracted from all the velocities of the nebula emission lines, the sky emission line shifts in that specific pointing and night. For the blue grism, we have used the 5198 \AA sky emission line since it is the only strong one detected. For the red grism, we have used the median shift of three strong sky lines that cover the wavelength range we are interested in: those at 6533.05 \AA , 6553.63 \AA , and 6863.97 \AA .

Finally, we have corrected the velocities to place them in the heliocentric or barycentric system. The corrections are near-identical for the two nights, -25.89 km s^{-1} the first one and -25.91 km s^{-1} the second one, using the routine

Table 2. Receding velocities and fluxes of the different emission lines in the nebula, for all four pointings and both nights. Missing values are due to lack of detection (except for P3 in the three reddest lines, where no observation was taken). Fluxes are computed integrating the best fitting Gaussian profile to each line. Note that line fluxes in the second night are considered less reliable due to flux calibration issues (see section 3.2.1). The velocities are presented in the barycentric reference system.

Emission line	Pointing	Velocity [km/s]		Flux [10 ⁻¹⁸ erg s ⁻¹ cm ⁻² arcsec ⁻²]
		D1	D2	D1
H β	P1	-27.9 \pm 2.0	-29.1 \pm 1.2	1.72 \pm 0.28
	P2	-31.3 \pm 1.4	-34.1 \pm 2.6	1.64 \pm 0.16
	P3		-25.3 \pm 2.7	1.68 \pm 0.12
	P4		-30.2 \pm 2.8	1.12 \pm 0.20
[O III]4959	P1		-6.9 \pm 4.7	
	P2	-13.6 \pm 2.7		0.56 \pm 0.12
	P3			
	P4			
[O III]5007	P1	-7.7 \pm 1.3	-12.4 \pm 2.3	2.44 \pm 0.24
	P2	-6.2 \pm 1.1	-10.4 \pm 1.9	2.04 \pm 0.16
	P3	-11.6 \pm 1.4	-10.7 \pm 2.8	1.88 \pm 0.16
	P4			
[N II]6583	P1	-20.1 \pm 1.9	-19.7 \pm 2.2	1.64 \pm 0.08
	P2	-29.4 \pm 1.6	-27.1 \pm 2.7	1.64 \pm 0.12
	P3			
	P4		-21.5 \pm 3.1	0.84 \pm 0.16
[S II]6716	P1	-20.2 \pm 2.4	-20.4 \pm 2.9	1.32 \pm 0.16
	P2	-27.7 \pm 2.5		1.44 \pm 0.12
	P3			
	P4	-20.2 \pm 2.4		1.12 \pm 0.12
[S II]6731	P1	-19.4 \pm 1.9	-18.1 \pm 3.7	0.96 \pm 0.12
	P2	-24.9 \pm 1.6		1.00 \pm 0.08
	P3			
	P4	-14.2 \pm 3.9	-13.11 \pm 5.3	0.88 \pm 0.16

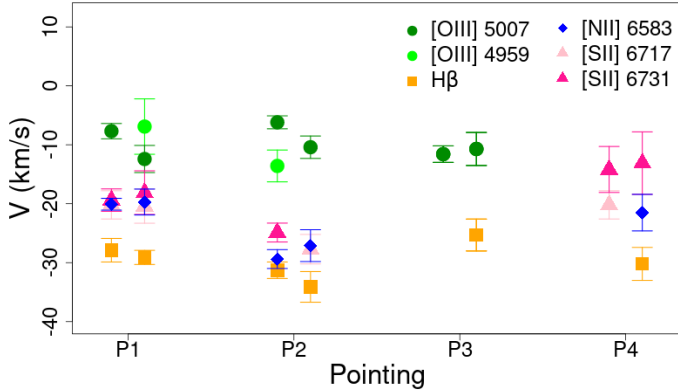


Fig. 5. Receding barycentric velocities derived from different emission lines and pointings. For each pointing, the first column corresponds to results from the first night of observations, and the second one to the second night. Color code and lines missing as in Fig. 4.

radial_velocity_correction from astropy (Astropy Collaboration et al. 2013, 2018, 2022).

We report the velocities and their uncertainties for all the nebula emission lines that are successfully fitted by our code in Table 2, and show them in Fig. 5.

3.2.3. Emission line widths

In order to further investigate the physical properties of the gas in the nebula, we have measured the width of the emission lines. More precisely, we report the standard deviation (σ) of the best-fitting Gaussian model for each line with the same code we used to measure the emission line velocities and fluxes. However, this measured width is the convolution of the intrinsic width of the line and the instrumental profile.

We can study the width of the sky emission lines in our data to get a direct measurement of the instrumental broadening effect. Their intrinsic line width is very small, below $\sigma=0.01$ Å in all the sky lines we detect (Hanuschik 2003), and therefore we can assume that the width we measure for them is essentially due to instrumental effects. We have measured the same sky emission lines mentioned in the previous subsection, and have obtained a very consistent width value, 19.30 ± 0.30 km s⁻¹. Separating by VPH, the difference is not striking: 19.70 ± 0.37 km s⁻¹ for the only sky line in LR-B, 5198 Å, and 19.2 ± 0.16 km s⁻¹ for the three lines considered in LR-R. This is reasonably consistent with the theoretical values (20.95 km/s and 21.20 km/s) obtained from the nominal spectral resolution of MEGARA VPHs². In the following analysis we consider as instrumental width the values derived from the sky emission lines.

In Table 3 we summarize the observed line widths, separating by different lines, but considering together for each line all the pointings in the nebula and both days. The uncertainties

² <https://www.gtc.iac.es/instruments/megara/>

Table 3. Width of emission lines

Emission line	Width [km s ⁻¹]
H β	22.0 \pm 1.4
[O III] 5007	21.9 \pm 1.0
Sky line 5198 Å	19.7 \pm 0.546
[N II] 6583	27.8 \pm 1.5
[S II] 6716, 6731	28.3 \pm 2.1
Sky line 6554 Å	19.10 \pm 0.05
Sky line 6864 Å	19.25 \pm 0.12

shown correspond to the dispersion in the width values measured for a particular line in the different pointings and in both days.

Finally, to de-convolve the instrumental effect from these widths, we apply the following equation:

$$\sigma_{int} = \sqrt{\sigma_{obs}^2 - \sigma_{inst}^2}$$

where σ_{int} is the intrinsic velocity dispersion, while σ_{obs} is the observed one and σ_{inst} is the instrumental dispersion. For σ_{obs} values very similar (considering uncertainties) to σ_{inst} we can only provide upper limits for σ_{int} . For H β and [O III], σ_{int} must be smaller than 17 km s⁻¹ and 19 km s⁻¹, respectively, considering 3 σ limits. The [N II] and [S II] emission line widths are however significantly (more than 4 σ) wider than the instrumental width, as traced by their nearby sky emission lines. Applying the equation, we obtain $\sigma_{int}=20.2 \pm 2.1$ km s⁻¹ for [N II], and $\sigma_{int}=20.7 \pm 3.1$ km s⁻¹ for [S II].

4. Discussion

In this Section we will review the results presented in this work, and compare them with the literature regarding different classes of nebula.

In Fesen et al. (2023), the authors reviewed in detail the evidence gathered about SDO, and considered whether it could belong to different categories of galactic structures. The apparent lack of H α emission and its size and location in the sky (suspiciously close to M31, and distant from the galactic plane), made the authors discard the possibilities of SDO belonging to the Milky Way. In the present Section, we will focus on the new results we obtain and compare them with Fesen et al. (2023) and other studies in the literature.

4.1. Kinematics of the nebula

4.1.1. Receding velocity

The receding velocity of the emission lines ranges from -6 km s⁻¹ to -30 km s⁻¹. The systemic velocity of M31 is -300 km s⁻¹, but in the area of the galaxy closer to the nebula (around half a degree away), the receding velocity of the stars and gas in M31 ranges from -400 to -250 km s⁻¹, according to different studies using optical spectroscopy or HI data (Opitsch et al. 2018; Corbelli et al. 2010).

In addition to the significant discrepancy with the M31 receding velocity, we find a remarkable consistency in velocity for the different lines across different pointings. For P1, P2, and P3, the three pointings on the [O III] nebula, the [O III]5007 velocity is consistent within 5.4 km s⁻¹, with a median uncertainty of 1.9 km s⁻¹ in each line. For H β , where it is detected, the range is 9

km s⁻¹ with an uncertainty of 3.2 km s⁻¹. The [S II] emission lines and [N II]6583 do show slightly higher discrepancies, of ~ 10 km s⁻¹ and a median uncertainty of 2 km s⁻¹. If the nebula were at a similar distance as M31 (770 kpc), this would mean a nearly constant velocity over distances of 6 kpc, and across different directions and filaments of the nebula. In M31, across a similar angular separation, the velocity change is closer to 200 km s⁻¹ (Opitsch et al. 2018; Corbelli et al. 2010).

We can compare the nebula with large Extended Emission Line Regions (EELRs) detected around distant galaxies (Lintott et al. 2009; Keel et al. 2012; Melso et al. 2024; Keel et al. 2024). First, these kind of nebulae are associated with AGN, while the M31 supermassive black hole remains mostly dormant (e.g. Peng et al. 2023). In addition, in most of the cases reported, the velocity of the gas in those EELRs follows a smooth progression from the systemic velocity of the galaxy up to that of the EELR (Keel et al. 2012). In the case of the first one discovered (Hanny’s Voorwerp), the EELR has a significant velocity difference compared to the galaxy, but it also shows a significant velocity gradient over just 1 kpc (Lintott et al. 2009). Many EELRs show similar velocity gradients, but a few show the same velocity over several kpcs (Keel et al. 2012).

In contrast, multiple structures containing ionized gas within our galaxy show emission line velocities consistent with our results (Flores-Durán et al. 2014). Given the difference in receding velocity between the different elements, it could be argued that they may belong to different physical structures, and they simply happen to be on the same line of sight by chance. Regarding this, recent observations by amateur astronomers (known as "The Deep Sky Collective"³) have targeted the nebula in multiple narrowbands⁴. In their Figure 6, using a [S II] filter, they have identified several “strands” that match very well the structure seen in [O III] emission. This supports our assumption that the [O III] and the [S II] emission are (at least in part) originated in the same physical structure, despite their difference in velocity. They also find some similarities between the distribution of H α and [O III]. We consider that this result, coupled with the similarity between the [S II] and [N II] velocities (and to some extent, H β) strengthens the hypothesis that most of the emission line flux we measure comes from the same nebula. In addition, there are examples in the literature of nearby nebulae in the Milky Way that also show differences in velocity for emission lines while belonging to the same structure, such as the Orion Nebula (Doi et al. 2004) or the observations of the interstellar medium (ISM) towards the Perseus arm (Madsen et al. 2006, their Fig. 9), where the peak of emission in different emission lines differs by tens of km s⁻¹. Another singular structure that shares some kinematic and morphological properties with SDO is Sh 2-174 (Sharpless 1959). This is an ionized gas cloud with a complex shape, which includes a region emitting mostly [O III], containing two near parallel arcs. It is surrounded to the south by a more amorphous H α emitting region. It was first reported in Sharpless (1959), and was also noted in Lynds (1965), but was first proposed to be a planetary nebula by Napiwotzki & Schonberger (1993). In Frew (2008) it is discussed in some detail, and also in Ransom et al. (2015). In particular, regarding the velocity of the emission lines, there is some separation but not as strong as in our case. The heliocentric velocities are -11.2 km s⁻¹ for H α , -7.3 km s⁻¹ for [O III]5007, and -15.0 km s⁻¹ for [N II], with uncertainties of 2 km s⁻¹ for all measurements.

³ <https://deepskycollective.com/home>

⁴ <https://www.astrobin.com/ymtvkr/F/>

Finally, we can compare our measurements to previous spectroscopic observations of SDO. Our pointing P1 is located just 90 arcsec to the west of Slit 2 placement in Fesen et al. (2023), allowing us to compare both measurements. Like them, we detect $H\beta$, [O III]4959, and [O III]5007. The heliocentric velocity we measure for [O III]5007 in both nights ($-7.5 \pm 1.9 \text{ km s}^{-1}$ the first one and $-6.7 \pm 2.3 \text{ km s}^{-1}$ the second) are perfectly compatible with their value of $-9.8 \pm 6.8 \text{ km s}^{-1}$, rendering more confidence to both our measurements. Their $H\beta$ determination, $+34 \pm 14 \text{ km s}^{-1}$, is however very different from ours, $-31.4 \pm 1.2 \text{ km s}^{-1}$, a 4.7σ discrepancy considering their measurement. The lower S/N of their $H\beta$ line and its wider profile may explain part of the discrepancy, along with the fact that their $H\beta$ measurement only takes in consideration around half of the size along the slit used in their [O III]5007 measurement (and while nearby, they do not overlap with our measurement).

Our results are not compatible however with those in Amram et al. (2023) on SDO. They measure a velocity of $-96 \pm 4 \text{ km s}^{-1}$ fitting all lines they detect: a 16σ discrepancy with our lowest velocity measured ($H\beta$). The source of this difference is not immediately obvious. The distances between our P1 region and their slit, 6.5 arcmin, is larger than the one separating Fesen et al. (2023) and P1, but it is still small compared to the distances between our pointings (almost 30 arcmin), and yet we find consistent velocities across the nebula. We must take into account that the resolution in Amram et al. (2023) is between 2.4 to 2.9 times lower than ours, resulting in broader sky emission lines, contaminating the $H\alpha$, [N II], and [S II] emission lines (their Fig. 2). In addition, their [O III] emission is contaminated by Sodium emission from urban street lights.

4.1.2. Emission line width

The typical width of the emission lines measured in the nebula is narrow, with velocity dispersions below 19 km s^{-1} for [O III]5007 or $H\beta$, and $\sim 20 \text{ km s}^{-1}$ for [N II] and [S II]. All of these widths are too low to be compatible with typical values measured in supernova remnants (SNR). In Points et al. (2019), Vicens-Mouret et al. (2023), or Duarte Puertas et al. (2024), no clear SNR has been found with $\sigma < 40 \text{ km s}^{-1}$. These values are however compatible with photoionized nebulae like H II regions, even in some cases in larger scales like on the EELR (Schweizer et al. 2013; Melso et al. 2024). The spectral properties of the Sh 2-174 nebula introduced in Section 4.1.1 also bear some resemblance to SDO. The width of the emission lines is $\sigma \sim 11 \text{ km s}^{-1}$, consistent with our measurements for [O III] and $H\beta$. This is however lower than the value measured in most planetary nebula.

The consistency within uncertainties between the width in the [O III]5007 and the $H\beta$ emission line widths, coupled with the similar fluxes and velocities measured across the nebula pointings, strengthens our hypothesis that both lines are generated at the same physical structure. The discrepancy in the width of the [N II] and [S II] emission lines points towards a more turbulent phase of the nebula being the source of this flux, but a full explanation would require multiple, deeper follow-up observations.

The small width of the emission lines also challenges possible explanations involving planetary nebulae or Wolf-Rayet nebulae. These objects are expanding shells of material, with typical double peaked line profiles with expansion velocities of a few tens of km s^{-1} (e.g. Chu et al. 1991; Montoro-Molina et al. 2023). In rare cases of very extended planetary nebula, the limb or only one side of the expanding shell may be detected, and thus

a single-peaked, narrower emission line may be detected. However, in that case, the smaller velocity dispersion we measure in $H\beta$ compared to [N II] would be unusual.

Finally, using the emission line widths, we can provide a rough estimate of the total mass and density of the nebula under the assumptions of uniformity and virial equilibrium. To estimate k , the scaling factor in the virial theorem, we assume an isothermal (smooth and diffuse) system, which results in $k = 1$. The nebula's area is approximated as 702 arcmin^2 , modeled as a trapezoid with bases of 60 arcmin and 18 arcmin, and a height of 18 arcmin. Assuming the depth of the nebula is equal to its height, we compute a total volume of $1.42 \times 10^{11} \text{ pc}^3$ if the nebula is located at a distance of 770 kpc, comparable to the distance of M31. For a velocity dispersion of 10 km s^{-1} (an approximation to that of $H\beta$ and [O III]), the resulting gas mass is $7.5 \times 10^8 M_\odot$. The corresponding density, assuming it is a fully ionized nebula of pure hydrogen, is $n_{\text{HII}} = 2.1 \times 10^{-2} \text{ cm}^{-3}$. This density would be comparable to some of the lowest-density gas in the Milky Way ($0.03\text{--}0.08 \text{ cm}^{-3}$ in Haffner et al. 2009), while other extragalactic ionized structures such as EELRs typically have densities of $10\text{--}100 \text{ cm}^{-3}$ (Keel et al. 2012). At a distance within the Milky Way halo (7 kpc), with $k = 1$ and a velocity dispersion of 10 km s^{-1} , the total volume would decrease to $1.1 \times 10^5 \text{ pc}^3$, and the gas mass would drop to $6.8 \times 10^5 M_\odot$. The corresponding density would be $n_{\text{HII}} = 2.6 \times 10^2 \text{ cm}^{-3}$. These values would be compatible with giant filaments in the ISM (Hacar et al. 2023), and also with the electron density we estimated for the nebula using the [S II] ratio. It is important to note that this calculations are just rough estimates, intended mainly to show the broad properties of SDO, depending on its location.

4.2. Emission line fluxes and ratios

The flux values in P1 and P2, despite being 27.8 arcmin apart, are similar in all emission lines ($H\beta$, [O III]5007, [N II], and [S II]). This can be extended to the P3 pointing in the nebula for [O III] and $H\beta$, the only emission lines targeted. In contrast, when we go beyond the position of the [O III] nebula in the Drechsler et al. (2023), in our P4 pointing, the $H\beta$, [N II], and [S II]6716 fluxes drop by $\sim 30 \%$. The [S II]6731 flux remain roughly constant, which results in a change in the [S II] ratio and thus in our inferred electron density. This suggests that the pointings in the nebula are consistent with each other, considering all emission lines, while P4 outside it is different. This supports the idea that the $H\beta$, [N II], and [S II] emissions in the P1, P2, and P3 pointings are physically related with the [O III] nebula.

The flux ratio [O III]5007/ $H\beta$ measured in the three pointings on the nebula (P1, P2, and P3) ranges from 1.42 to 1.12. These values are consistent with several galactic structures, such as planetary nebulae, H II regions (Frew & Parker 2010), and diffuse ionized gas (DIG, González-Díaz et al. 2024). In contrast, the ratios measured in EELRs in distant galaxies are significantly higher (Keel et al. 2012, 2024). Without accurate $H\alpha$ flux measurements, we cannot directly calculate the [N II]/ $H\alpha$ or [S II]/ $H\alpha$ ratios. However, knowing the $H\beta$ values, and assuming Case B recombination with $T_e = 10\,000 \text{ K}$ and $n_e = 10^{-3}$ (Osterbrock & Ferland 2006), we know that $F_{H\alpha} \geq 2.86 F_{H\beta}$, with $F_{H\alpha}$ being higher with higher dust extinction. Considering this, we obtain mean values of $\log_{10}([\text{N II}]/H\alpha) = -0.313 \pm 0.038$ and $\log_{10}([\text{S II}]/H\alpha) = -0.469 \pm 0.038$ for the P1 and P2 pointings. With these ratios, we can find that our nebula is located in the limit of planetary nebulae in Figure 4 of Frew & Parker (2010), going into the region where most of their H II regions and Wolf-Rayet nebulae lie.

The [S II]6716/[S II]6731 ratios are 1.37 and 1.44 in P1 and P2, respectively, and can be used to estimate physical properties as well, especially electron density. Given the large uncertainties in the ratios (the 1σ limits go from 1.175 to 1.600), the precision is relatively low, but we can estimate that the density is below 300 cm^{-3} (assuming electronic temperatures from 5000 K to 20 000 K). These densities are consistent with planetary nebulae, H II regions, some supernova remnants (Celnik et al. 2024) as well as EELRs (Keel et al. 2012). These ratios could provide additional help distinguishing between them, but in this case SDSS shows values close to the three classes of structures (see Figure 11 in Celnik et al. 2024).

The [S II]/[N II] ratios can be measured in P1 and P2 in the nebula, giving values of 0.80 ± 0.11 and 0.88 ± 0.10 . According to González-Díaz et al. (2024) these values are relatively typical for DIG, in areas that show [O III]5007/H β ratios that are also consistent with our measurements. They are found at not very large distances from the ionizing source (in galactic scales, i.e. $\sim \text{kpc}$).

We can also compare some of our flux measurements with previous observations of the nebula. The [O III]5007 emission line flux is consistent with what was estimated by Drechsler et al. (2023) in the photometry and by Fesen et al. (2023) in both photometry and spectroscopy. More specifically, in our aperture P1 (located only 90 arcsec to the west of Slit 2 in Fesen et al. 2023) we measure a line surface brightness of $(2.45 \pm 0.24) \cdot 10^{-18} \text{ erg s}^{-1} \text{ cm}^{-2} \text{ arcsec}^{-2}$, compatible with their measurement of $(4 \pm 2) \cdot 10^{-18} \text{ erg s}^{-1} \text{ cm}^{-2} \text{ arcsec}^{-2}$.

We find a stronger H β emission than what Fesen et al. (2023) find in their Slit 2, where it seems roughly [O III]5007/H $\beta \sim 2.5$, and our closer pointing P1 shows [O III]5007/H $\beta = 1.42$. This difference may be due to the physical locations explored being slightly different, considering also that relatively large areas are being integrated together, and that the S/N is relatively low.

Our measurements for the [O III]5007/H β ratio in the different locations (or even the spectrum in Slit 2 in Fesen et al. 2023) are in clear contrast with the estimations made based on the photometry of [O III]/H $\alpha > 5$ (Drechsler et al. 2023; Fesen et al. 2023). If [O III]5007/H $\beta \sim 2.5$, and considering that for typical conditions of the ISM and no extinction, H α /H $\beta = 2.95$, then [O III]/H α must be at most 0.85. In P3, this would go as low as 0.38. Using the dustmaps code (Green 2018), we find little evidence of significant dust extinction, with values of $E(B-V) \sim 0.06$ for all pointings in the nebula.

We can also indirectly compare our JAST80 photometric data to the MEGARA line fluxes. Since we have no H α spectroscopic measurements, we have to rely in its relation to H β ($H\alpha \geq 2.86 \cdot H\beta$, as stated earlier in this Section). We must also include [N II]6583, which falls within the wavelength range of J0660. This results in an estimated flux in P1 $\geq (6.72 \pm 0.88) \cdot 10^{-18} \text{ erg s}^{-1} \text{ cm}^{-2} \text{ arcsec}^{-2}$. The average surface brightness we measure in the J0660 detection is $(5.50 \pm 1.0) \cdot 10^{-18} \text{ erg s}^{-1} \text{ cm}^{-2} \text{ arcsec}^{-2}$, compatible with the spectroscopic value in P1 (assuming very low dust extinction, as mentioned before).

A more complex comparison could be performed with the J0378 image tracing [O II]3727 emission. Surface brightness measurements in the two elongated structures are $(8.1 \pm 1.6) \cdot 10^{-18} \text{ erg s}^{-1} \text{ cm}^{-2} \text{ arcsec}^{-2}$ and $(6.2 \pm 1.1) \cdot 10^{-18} \text{ erg s}^{-1} \text{ cm}^{-2} \text{ arcsec}^{-2}$. As a first approximation, these would result in a [O III]/[O II] ratio around 0.3. This value can be reached in typical galaxies (Perrotta et al. 2021; Paalvast et al. 2018), and also in DIG (Galarza et al. 1999; Zhang et al. 2017), but it is very different from the values measured in EELRs, typically from 2 to 6 (Lintott et al. 2009; Keel et al. 2012).

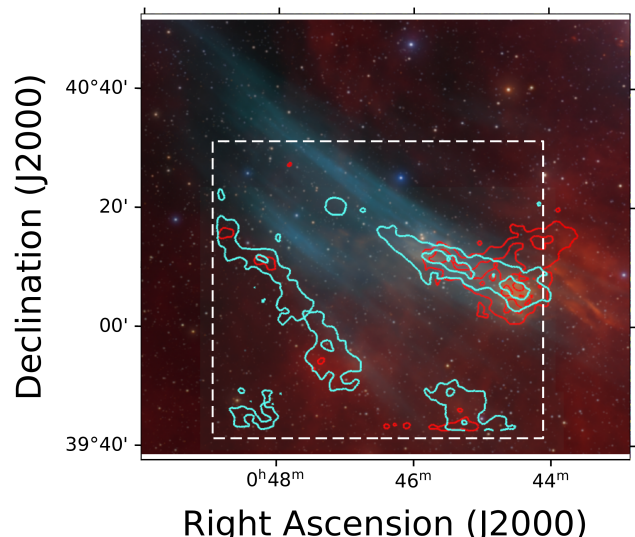


Fig. 6. Contours of emission in the JAST80 observations on the nebula, for [O II] (filter J0378) in cyan, and for H α in red (filter J0660). The dashed-line square represents the region with full depth in the JAST80 images. In the background, the RGB composition shown in Fig 1 and presented in Drechsler et al. (2023), with red tracing H α and cyan [O III].

4.3. Morphology

The main result identified in the OAJ narrowband imaging data has been the near-parallel emission line stripes in the [O II] 3727 emission image (traced with the J0378 filter). The position of these stripes does not match the position of the regions with emission in [O III] as traced in Drechsler et al. (2023), which we show in Fig. 6.

The brightest one (on the right) partially overlaps with the brightest part of the main strand of the [O III] nebula, and then, in its easternmost part, it separates slightly to the south. It makes a small angle of $\sim 17^\circ$ with the [O III] emission, and ends over the secondary structure of the main [O III] strand. The fainter region in our [O II] image is near to the fainter [O III] strand, but also shows a significant separation towards the south. This separation reaches a minimum value of 6.5 arcmin between the brightest points of the regions in their nearest point. They both follow roughly the same south-east direction like the other [O II] and [O III] strands, also making a small angle (14°), but this time in the opposite direction.

Significant angular separation between the regions where the maximum flux of emission lines is located can be observed in nearby nebulae. This only occurs if they are either close enough or large enough for its stratification structure to be resolved. In Barman et al. (2022), they show an example with a separation of $\sim 4 \text{ pc}$. If we look at the distance between peaks of [O III] and [S II] emission, in Pellegrini et al. (2012) these values can be higher, up to 20 to 25 pc. In one of the largest H II regions in the local group (NGC604 in M33), with *Hubble Space Telescope* data (P.I. Barbá R.)⁵ presented in Barbá et al. (2009), we measure $\sim 4 \text{ pc}$ separation between [O III] and [O II] strands.

In our case, even if the physical distance was in the large end of the range (25 pc), the resulting angular separation would be of just 6.63 arcsec at the distance of M31, 500 times smaller than what we see in our images. Considering this range of physical separation (from 4 to 25 pc), in order to match the 6 arcmin

⁵ https://archive.stsci.edu/proposal_search.php?id=10419&mission=hst

separation we measure between the [O III] and [O II] emitting strands, the physical distance to the nebula would be between 2 and 14 kpc. These values would place the object well within the Milky Way.

The Sh 2-174 nebula we introduced in Section 4.1.1 also shows some morphological similarities to SDO. It was first considered as a planetary nebula (Napiwotzki & Schonberner 1993) but later analysis by Frew (2008) pointed towards it being an H II region: the lack of limb brightening in the edges, the narrow width of the emission lines, and the difference in velocity between its "central" star and the gas. Subsequently, using radio data, Ransom et al. (2015) presented evidence that it is in fact a planetary nebula that has interacted with a cloud of neutral hydrogen.

The most detailed images of Sh 2-174 available have likely been produced by amateur astronomers using narrowband filters (for example, the image⁶ by R. Shepard with red for H α and blue-turquoise for [O III]). In those images Sh 2-174 shows three narrow, near-parallel strands of [O III] emission, very similar to the ones in this nebula (Fig. 6). In addition, the H α emission is physically separated from these [O III] strands, with the ionizing star of the nebula (GD 561, a white dwarf) located roughly in between. The H α emission shows a morphology different to [O III], presenting an area with thinner, brighter strands with more small-scale structure near the [O III] emission, and a broader, smoother region beyond. Those characteristics are also similar to what we see in H α in SDO images, even if the precise morphology does not match. The separation between the peaks of emission in [O III] and H α is around 7 arcmin, which, given the distance of 290 pc to Sh 2-174 (Gaia Collaboration 2020), translates into ~ 0.6 pc. We note that these similarities do not necessarily mean that the physical processes that originate the properties of Sh 2-174 are the same as those behind SDO. Rather, we just show that there are small structures within the Milky Way that share characteristics with SDO, whereas we have not found suitable extragalactic counterparts.

Finally, we can discuss the general structure of SDO in [O III]. It is very elongated and composed of several strands, with axis ratios around 10:1, depending on where the separations are placed. Its surface brightness distribution is smooth, without presenting areas much brighter than others. The smoothness is also seen in other galactic structures, such as Sh 2-174 or filaments (Hacar et al. 2023). However, large extragalactic ionized structures like EELRs show a more intricate and rough morphology. Regarding its size, ISM filaments span a wide range of physical sizes, from 0.1 to 200 pc (Hacar et al. 2023). This would place SDO, given its ~ 1.5 deg of angular size, between 3.8 pc and 7.6 kpc away. This is a very poorly constrained estimation, but it confirms that it could be a galactic filament given its angular size.

4.4. Physical nature of the nebula

In the previous sections, we have discussed the available physical measurements of the [O III] nebula, and compared them with the properties of other classes of objects to constrain its location and characteristics.

The kinematical evidence strongly supports the galactic nature of SDO. First, the receding velocity we measure is not compatible with the velocity of gas and stars in M31, especially in the region closer to the nebula. In addition, the velocities measured for a given emission line across all pointings are remark-

ably consistent. This is not surprising if the nebula was within our Galaxy, and the distances between pointings were in the order of tens of parsecs, but it would be rare for an extragalactic cloud of gas across several kiloparsecs.

The emission lines are narrow, with velocity dispersion below 20 km s^{-1} in H β and [O III]. This makes it very unlikely that the nebula is part of a SNR or stellar ejecta. Shock ionization, which has been considered the most likely source of ionization for SDO in Fesen et al. (2023), is likely incompatible with this result, since it requires velocity dispersions above 80 km s^{-1} (Kewley et al. 2019 and references therein). The width of the emission lines also allows us to make rough estimates of the total mass and density of the nebula. If it were located at the distance of M31, it would be very massive (almost $\sim 10^8 M_{\odot}$), requiring very a strong ionizing source like an AGN. Moreover, it would have a very low density ($\sim 0.03 \text{ cm}^{-3}$). This combination is unlikely, given the lack of AGN activity in M31 (e.g. Peng et al. 2023) and the electron density of EELRs being $10^3 - 10^4$ times higher. In contrast, if it were within the Milky Way, its derived properties (mass $\sim 10^5 M_{\odot}$ and density $\sim 10^2 \text{ cm}^{-3}$) would be more in line with other known objects, like giant filaments (Hacar et al. 2023).

The emission line ratios measured are compatible with multiple Milky Way structures (ISM filaments, planetary nebula, H II regions), with the [S II]6716/[S II]6731 ratios indicating an electron density below 300 cm^{-3} . In contrast, the [O III]5007/H β ratio is too low to be compatible with EELRs, one of the few known large ionized structures around external galaxies. In addition, these structures may show characteristic features in other parts of the electromagnetic spectrum. The original Hanny's Voorwerp has been identified in radio data from the LOw Frequency ARray (LOFAR, Smith et al. 2022). Visual inspection of the LOFAR data on SDO (Shimwell et al. 2022) shows no emission, an additional piece of evidence against its EELR-like nature.

Finally, the angular separation between the emission in [O II] and [O III] can be observed in other gas clouds, but it would be too small to be visible if the nebula were located at extragalactic distances. The separation between ionized species can be seen also in the Sh 2-174 galactic nebula discussed earlier, with [O III] filaments separated from H α diffuse emission.

Considering the evidence we have gathered and presented, our most compelling explanation is that the nebula belongs to the ISM of the Milky Way, probably to its diffuse phase. Given its morphology, the nebula may be considered an ISM filament. As stated in Fesen et al. (2023), most of these filaments are detected in radio or infrared, with only a few having optical emission line observations, almost always with H α (McCullough & Benjamin 2001; West et al. 2022). Nevertheless, this may not be a physical necessity, but just due to a lack of spectroscopic follow-up observations on galactic filaments targeting other emission lines. Deep photometric narrowband surveys other than in H α are certainly missing, as proven by Drechsler et al. (2023), discovering such a large structure in an area of the sky surveyed for more than 100 years. Despite that, there are some indications that these H α filaments may have some [O III] emission, such as some of the high galactic latitude structures in Madsen et al. (2006).

Moreover, the lack of change in velocity across SDO is also consistent with the velocity gradients measured in galactic filaments. In Hacar et al. (2023), typical values of gradients and lengths can result in velocity shifts of at most a few km s^{-1} , and as low as less than 1 km s^{-1} , as shown also in Wang et al. (2024).

Finally, some evolved star ejecta may also create filament-like features, with separated [O III] and H α emitting regions,

⁶ <https://www.astrobin.com/4mafcb/0/>

like those shown in Garnett & Chu (1994); Gruendl et al. (2000); Stupar et al. (2010). However, cases with [O III] detached from $H\alpha$ are often caused by the expansion of a shock within a lower density medium, an effect that can be seen as well in planetary nebulae (Guerrero et al. 2013). Nevertheless, in those cases the morphology is often very sharp, in contrast with SDO.

In summary, the nebula shows mixed properties, some in the edge of different classes of objects, and no clear ionizing source has been identified. The absence of a clearly determined source for the ionization is common in gas filaments in the Milky Way and in the DIG in external galaxies. For the latter, multiple sources have been proposed: leaking photons from OB star associations; low mass, hot, evolved stars (HOLMES, Pérez-Montero et al. 2023); shocks; cosmic rays, etc. (González-Díaz et al. 2024). Considering other studies of the DIG, such as Weber et al. (2019), some of the line ratios we measure are consistent with that explanation ([O III]/[O II], [O III]5007/ $H\beta$), but others would be inconsistent (e.g. [S II]/[N II] would be around 0.8, higher than the nebula). Other studies, such as Zhang et al. (2017); Koutsoumpou et al. (2024), consider cosmic rays as an additional source for DIG ionization, and show line ratios compatible with the ones we measure in the nebula. Some of the DIG ionization methods discussed here may be the additional ionizing source responsible for the [O III] emission we found in SDO, a relatively uncommon feature in a typical Milky Way filament. Still, with the data gathered up to now we cannot determine precisely to which class of objects the nebula belongs to.

5. Conclusions

In this work, we have presented new observations, both spectroscopic and photometric, on the recently discovered large [O III] nebula along a line of sight close to M31. The spectra consisted on four pointings of the MEGARA IFU, mounted at the 10.4m GTC, while the photometry was obtained with narrowband filters tracing [O II] and $H\alpha$ and [N II] emission lines with the JAST80 telescope at the OAJ. The analysis of the data provides clear evidence that the object is not physically close to M31, but it is within our Milky Way instead. The key pieces of evidence are:

- The receding velocity of all emission lines measured in all MEGARA pointings within the nebula show values higher than -40 km s^{-1} , very different from the receding velocity of M31, -300 km s^{-1}
- The receding velocities measured for a given emission line in the different pointings on the nebula are very consistent, within a few km s^{-1} . This is normal in Milky Way structures of a few tens of parsecs of size, but uncommon in extragalactic gas extending over several kiloparsecs.
- The velocity dispersion of the emission lines (below 20 km s^{-1} for $H\beta$ and [O III]5007) is too low for shock ionization. Moreover, it suggests that, if SDO were located in the Milky Way, the mass and density of the nebula would be consistent with giant ISM filaments. At the distance of M31, however, it would be very massive and with extremely low density, inconsistent with EELRs.
- The [O III]5007/ $H\beta$ line ratios we measure in the nebula pointings (from 1.12 to 1.4) are consistent with several galactic structures, but they are much lower than what is typical in EELRs, the most well studied extragalactic [O III]-emitting gas clouds.

- In contrast with previous analysis, we identify clear hydrogen emission ($H\beta$) across the nebula. This makes the nebula more compatible with several structures within our galaxy, such as filaments or DIG.
- In the narrowband images tracing [O II] we detect two strands of emission near the [O III] nebula, with similar orientation, but with a ~ 7 arcmin shift. This is easy to explain if the [O II] strands are part of the nebula, and the separation is of just a few pc, making the SDO a Milky Way object.

We have presented compelling evidence demonstrating the location of the nebula within the Milky Way, but its precise nature and the class of objects it belongs to is less clear. Considering the line ratios ([O III]5007/ $H\beta$, [S II]/[N II], [S II]6716/[S II]6731), the lack of an evident source for the ionization, its filamentary morphology, and the width of the emission lines ($< 20 \text{ km s}^{-1}$ for [O III] and $H\beta$), the most fitting category to place the nebula is that of galactic ISM filaments.

Further spectroscopic analysis, on other locations in and around the nebula and covering bluer wavelengths, will help shed light onto its physical nature. The discovery and analysis of this object highlight the importance of observing wide fields of the sky with narrowband filters, as shown in Fesen et al. (2024). Large scale surveys of the sky in narrowband filters, such as J-PLUS (Cenarro et al. 2019) and especially the deeper J-PAS (Bonoli et al. 2021) will open a new window into the emission-line sky.

Acknowledgements. ALC would like to thank Asier Castrillo and Raúl González-Díaz for useful discussions. The authors would like to thank the team of OAJ operators responsible for the photometric observations, as well as the GTC team responsible for the spectroscopic observations. ALC, JAFO, AHC acknowledge financial support by the Spanish Ministry of Science and Innovation (MCIN/AEI/10.13039/501100011033), by “ERDF A way of making Europe” and by “European Union NextGenerationEU/PRTR” through the grants PID2021-124918NB-C44 and CNS2023-145339; MCIN and the European Union – NextGenerationEU through the Recovery and Resilience Facility project ICTS-MRR-2021-03-CEFCA. RIS acknowledges financial support from the Spanish Ministry of Science and Innovation through the project PID2022-138896NA-C54. HVA is supported by the grant PTA2021-020561-I, funded by MICIU/AEI/10.13039/501100011033 and by ESF+. AE acknowledges the financial support from the Spanish Ministry of Science and Innovation and the European Union - NextGenerationEU through the Recovery and Resilience Facility project ICTS-MRR-2021-03-CEFCA. This work was partly done using GNU Astronomy Utilities (Gnuastro, ascl.net/1801.009) version 0.23. Work on Gnuastro has been funded by the Japanese Ministry of Education, Culture, Sports, Science, and Technology (MEXT) scholarship and its Grant-in-Aid for Scientific Research (21244012, 24253003), the European Research Council (ERC) advanced grant 339659-MUSICOS, the Spanish Ministry of Economy and Competitiveness (MINECO, grant number AYA2016-76219-P) and the NextGenerationEU grant through the Recovery and Resilience Facility project ICTS-MRR-2021-03-CEFCA and the Spanish research agency grant PID2021-124918NA-C43. This work made use of Astropy⁷: a community-developed core Python package and an ecosystem of tools and resources for astronomy (Astropy Collaboration et al. 2022).

References

- Akhlaghi, M. 2019a, arXiv e-prints, arXiv:1909.11230
Akhlaghi, M. 2019b, in *Astronomical Society of the Pacific Conference Series*, Vol. 521, *Astronomical Data Analysis Software and Systems XXVI*, ed. M. Molinaro, K. Shorridge, & F. Pasian, 299
Akhlaghi, M. & Ichikawa, T. 2015, *ApJS*, 220, 1
Amram, P., Adam, C., Epinat, B., & Chemin, L. 2023, *A&A*, 671, L13
Astropy Collaboration, Price-Whelan, A. M., Lim, P. L., et al. 2022, *ApJ*, 935, 167
Astropy Collaboration, Price-Whelan, A. M., Sipőcz, B. M., et al. 2018, *AJ*, 156, 123

⁷ <http://www.astropy.org>

- Astropy Collaboration, Robitaille, T. P., Tollerud, E. J., et al. 2013, *A&A*, 558, A33
- Bacon, R., Conseil, S., Mary, D., et al. 2017, *A&A*, 608, A1
- Bacon, R., Mary, D., Garel, T., et al. 2021, *A&A*, 647, A107
- Barbá, R. H., Maíz Apellániz, J., Pérez, E., et al. 2009, *Ap&SS*, 324, 309
- Barman, S., Neelamkudan, N., Madden, S. C., et al. 2022, *ApJ*, 930, 100
- Benítez, N., Dupke, R., Moles, M., et al. 2014, *arXiv e-prints*, arXiv:1403.5237
- Bonoli, S., Marín-Franch, A., Varela, J., et al. 2021, *A&A*, 653, A31
- Cardamone, C. N., van Dokkum, P. G., Urry, C. M., et al. 2010, *ApJS*, 189, 270
- Celnik, W. E., Karachentsev, I., Köchling, P., et al. 2024, *arXiv e-prints*, arXiv:2402.05658
- Cenarro, A. J., Moles, M., Cristóbal-Hornillos, D., et al. 2019, *A&A*, 622, A176
- Chu, Y.-H., Manchado, A., Jacoby, G. H., & Kwitter, K. B. 1991, *ApJ*, 376, 150
- Corbelli, E., Lorenzoni, S., Walterbos, R., Braun, R., & Thilker, D. 2010, *A&A*, 511, A89
- Courtes, G. 1952, *Publications of the Observatoire Haute-Provence*, 2
- Danieli, S., Kado-Fong, E., Huang, S., et al. 2024, *arXiv e-prints*, arXiv:2410.01884
- Dennison, B., Simonetti, J. H., & Topasna, G. A. 1998, *PASA*, 15, 147
- Doi, T., O'Dell, C. R., & Hartigan, P. 2004, *AJ*, 127, 3456
- Drechsler, M., Strottner, X., Sainty, Y., et al. 2023, *Research Notes of the American Astronomical Society*, 7, 1
- Drew, J. E., Greimel, R., Irwin, M. J., et al. 2005, *MNRAS*, 362, 753
- Duarte Puertas, S., Drissen, L., Robert, C., et al. 2024, *MNRAS*, 533, 2677
- Dutta, R., Fumagalli, M., Fossati, M., et al. 2024, *arXiv e-prints*, arXiv:2409.02182
- Fesen, R. A., Drechsler, M., Strottner, X., et al. 2024, *ApJS*, 272, 36
- Fesen, R. A., Kimeswenger, S., Shull, J. M., et al. 2023, *ApJ*, 957, 82
- Flores-Durán, S. N., Peña, M., Hernández-Martínez, L., García-Rojas, J., & Ruiz, M. T. 2014, *A&A*, 568, A82
- Frew, D. J. 2008, PhD thesis, Macquarie University, Department of Physics and Astronomy
- Frew, D. J. & Parker, Q. A. 2010, *PASA*, 27, 129
- Gaia Collaboration. 2020, *VizieR Online Data Catalog: Gaia EDR3 (Gaia Collaboration, 2020)*, *VizieR On-line Data Catalog: I/350*. Originally published in: 2021A&A...649A...1G; doi:10.5270/esa-lug
- Galarza, V. C., Walterbos, R. A. M., & Braun, R. 1999, *AJ*, 118, 2775
- Garnett, D. R. & Chu, Y.-H. 1994, *PASP*, 106, 626
- Gondhalekar, Y., Chies-Santos, A. L., de Souza, R. S., et al. 2024, *MNRAS*, 532, 270
- González-Díaz, R., Rosales-Ortega, F. F., & Galbany, L. 2024, *arXiv e-prints*, arXiv:2406.17123
- Green, G. 2018, *The Journal of Open Source Software*, 3, 695
- Gruendl, R. A., Chu, Y.-H., Dunne, B. C., & Points, S. D. 2000, *AJ*, 120, 2670
- Guerrero, M. A., Toalá, J. A., Medina, J. J., et al. 2013, *A&A*, 557, A121
- Gum, C. S. 1953, *The Observatory*, 73, 123
- Hacar, A., Clark, S. E., Heitsch, F., et al. 2023, in *Astronomical Society of the Pacific Conference Series*, Vol. 534, *Protostars and Planets VII*, ed. S. Inutsuka, Y. Aikawa, T. Muto, K. Tomida, & M. Tamura, 153
- Haffner, L. M., Dettmar, R. J., Beckman, J. E., et al. 2009, *Reviews of Modern Physics*, 81, 969
- Haffner, L. M., Reynolds, R. J., Tufte, S. L., et al. 2003, *ApJS*, 149, 405
- Hanuschik, R. W. 2003, *A&A*, 407, 1157
- Infante-Sainz, R., Trujillo, I., & Román, J. 2020, *MNRAS*, 491, 5317
- Keel, W. C., Chojnowski, S. D., Bennert, V. N., et al. 2012, *MNRAS*, 420, 878
- Keel, W. C., Moiseev, A., Uklein, R., & Smirnova, A. 2024, *MNRAS*, 530, 1624
- Kewley, L. J., Nicholls, D. C., & Sutherland, R. S. 2019, *ARA&A*, 57, 511
- Kobayashi, C., Karakas, A. I., & Lugaro, M. 2020, *ApJ*, 900, 179
- Koutsoumpou, E., Fernández-Ontiveros, J. A., Dasyra, K. M., & Spinoglio, L. 2024, *arXiv e-prints*, arXiv:2411.17811
- Lintott, C. J., Schawinski, K., Keel, W., et al. 2009, *MNRAS*, 399, 129
- Lumbreras-Calle, A., López-Sanjuán, C., Sobral, D., et al. 2022, *A&A*, 668, A60
- Lynds, B. T. 1965, *ApJS*, 12, 163
- MacAlpine, G. M., Smith, S. B., & Lewis, D. W. 1977, *ApJS*, 34, 95
- Madsen, G. J., Reynolds, R. J., & Haffner, L. M. 2006, *ApJ*, 652, 401
- Markaryan, B. E. 1967, *Astrofizika*, 3, 55
- McCullough, P. R. & Benjamin, R. A. 2001, *AJ*, 122, 1500
- Melso, N., Schiminovich, D., Sitaram, M., et al. 2024, *ApJ*, 974, 161
- Mendes de Oliveira, C., Ribeiro, T., Schoenell, W., et al. 2019, *MNRAS*, 489, 241
- Minkowski, R. 1946, *PASP*, 58, 305
- Moles, M., Benítez, N., Aguerri, J. A. L., et al. 2008, *AJ*, 136, 1325
- Montoro-Molina, B., Guerrero, M. A., Santamaría, E., et al. 2023, *MNRAS*, 524, 1601
- Napiwotzki, R. & Schonberger, D. 1993, in *IAU Symposium*, Vol. 155, *Planetary Nebulae*, ed. R. Weinberger & A. Acker, 495
- Opitsch, M., Fabricius, M. H., Saglia, R. P., et al. 2018, *A&A*, 611, A38
- Osterbrock, D. E. & Ferland, G. J. 2006, *Astrophysics of gaseous nebulae and active galactic nuclei (University Science Books)*
- Paalvast, M., Verhamme, A., Straka, L. A., et al. 2018, *A&A*, 618, A40
- Parker, R. A. R., Gull, T. R., & Kirshner, R. P. 1979, *An emission-line survey of the Milky Way*, Vol. 434 (NASA-Washington, Scientific and Technical Information)
- Pascual, S., Cardiel, N., Picazo-Sanchez, P., Castillo-Morales, A., & Gil De Paz, A. 2021, *guai-x-ucm/megaradrp: v0.11*
- Pellegrini, E. W., Oey, M. S., Winkler, P. F., et al. 2012, *ApJ*, 755, 40
- Peng, S., Li, Z., Sjouwerman, L. O., et al. 2023, *ApJ*, 953, 12
- Pérez-González, P. G., Cava, A., Barro, G., et al. 2013, *ApJ*, 762, 46
- Pérez-Montero, E., Zinchenko, I. A., Vilchez, J. M., et al. 2023, *A&A*, 669, A88
- Perrotta, S., George, E. R., Coil, A. L., et al. 2021, *ApJ*, 923, 275
- Points, S. D., Long, K. S., Winkler, P. F., & Blair, W. P. 2019, *ApJ*, 887, 66
- Rahna, P. T., Zheng, Z. Y., Chies-Santos, A. L., et al. 2022, *A&A*, 668, A148
- Ransom, R. R., Kothes, R., Geisbuesch, J., Reich, W., & Landecker, T. L. 2015, *ApJ*, 799, 198
- Schweizer, F., Seitzer, P., Kelson, D. D., Villanueva, E. V., & Walth, G. L. 2013, *ApJ*, 773, 148
- Shajn, G. A. & Gaze, V. F. 1952, *Atlas Diffuznykh Gazovykh Tumannostei (Moscow: Academy of Sciences of USSR)*
- Sharpless, S. 1959, *ApJS*, 4, 257
- Shimwell, T. W., Hardcastle, M. J., Tasse, C., et al. 2022, *A&A*, 659, A1
- Smith, D. J. B., Krause, M. G., Hardcastle, M. J., & Drake, A. B. 2022, *MNRAS*, 514, 3879
- Stupar, M., Parker, Q. A., & Filipović, M. D. 2010, *MNRAS*, 401, 1760
- Taniguchi, Y., Kajisawa, M., Kobayashi, M. A. R., et al. 2015, *PASJ*, 67, 104
- Vicens-Mouret, S., Drissen, L., Robert, C., et al. 2023, *MNRAS*, 524, 3623
- Wang, K., Ge, Y., & Baug, T. 2024, *A&A*, 686, L11
- Weber, J. A., Pauldrach, A. W. A., & Hoffmann, T. L. 2019, *A&A*, 622, A115
- West, J. L., Campbell, J. L., Bhaura, P., et al. 2022, *ApJ*, 941, 6
- Wisotzki, L., Bacon, R., Brinchmann, J., et al. 2018, *Nature*, 562, 229
- Zhang, K., Yan, R., Bundy, K., et al. 2017, *MNRAS*, 466, 3217